Acta Crystallographica Section A
Foundations of Crystallography
ISSN 0108-7673

Received 16 May 2005
Accepted 29 September 2005

Ultra-small-angle X-ray scattering from dislocation structures

G. G. Long* and L. E. Levine

Materials Science and Engineering Laboratory, National Institute of Standards and Technology, Gaithersburg, MD 20899, USA. Correspondence e-mail: gglong@aps.anl.gov

Ultra-small-angle X-ray scattering data were obtained from deformed single-crystal aluminium samples. These data are consistent with recent theoretical predictions of scattering from dislocation walls, allowing quantitative microstructural parameters to be extracted.

1. Introduction

Among the earliest small-angle scattering (SAS) experiments to investigate the formation of dislocations was an attempt to study the scattering by structures in cold-worked metals. This (Blin & Guinier, 1951, 1953) and many subsequent attempts (Hayes & Smoluchowski, 1954; Beeman *et al.*, 1957; Atkinson & Lowde, 1957; Christ, 1964; Taglauer, 1968; Kettunen *et al.*, 1981; Lepistö *et al.*, 1991; Heuser, 1994) met with limited success for a variety of reasons. The most persistent difficulty was the intrusion of higher-contrast processes such as double Bragg diffraction. Other considerations include the angular dependence of the dislocation scattering, the importance of which was not fully appreciated at the time, and the possibility of observing surface scattering.

A study by Heuser (1994) made use of small-angle neutron scattering (SANS) to study single-crystal Cu samples deformed *ex situ*. At the lowest scattering vector, $\mathbf{q}$ [where $|\mathbf{q}| = (4\pi/\lambda)\sin(\theta)$, λ is the neutron wavelength and 2θ is the scattering angle], obtainable in this experiment (0.0065 Å^{-1}), Heuser reported a q^{-2} slope, which is consistent with predictions of the scattering form factor for individual dislocations (Seeger, 1959*b*). Heuser's work demonstrated that dislocations could be detected by means of SANS from cold-worked samples. To take the next step and obtain quantitative data on such structures, several additional difficulties remained to be overcome.

The first requirement was the development of a theory for the SAS from dislocation walls. Although much work has been done on the theory of SAS from individual dislocations (Dexter, 1953; Seeger, 1959*a*,*b*; Seeger & Brand, 1965), none of these studies considered scattering by dislocations arranged in walls. A theory of scattering from such arrangements is now available (Thomson *et al.*, 1999), allowing the design of SAS experiments that optimize the observability of the dislocation-wall scattering features while avoiding undesirable scattering processes. The new theory has the further advantage of enabling quantitative microstructural parameters to be extracted from the scattering data.

Consideration of the various length scales involved leads to the conclusion that a q range extending below 10^{-3} Å^{-1} with a $\Delta q \leq 10^{-4}$ Å^{-1} is required for these experiments. Thus, ultra-small-angle X-ray scattering (USAXS) and ultra-small-angle neutron scattering (USANS) are potential candidates. USAXS experiments using $\approx$1.76 Å photons can be performed in a manner that avoids Bragg diffractions by adjusting the single-crystal sample orientation. This wavelength also allows the use of samples that are thick enough to represent bulk material ($\approx$0.2 mm).

In the following sections, we present a brief overview of the dislocation SAS theory, describe the experiments, discuss the measures taken to avoid the difficulties mentioned above and present experimental data for comparison with the theoretical predictions.

2. SAS theory

Small-angle scattering by dislocations is caused exclusively by the small local density change induced by the dislocations. Several effects contribute to this density change including the elastic dilation, density changes in the core and the nonlinear part of the elastic field. Because the elastic dilation dominates in the q range where dislocation wall structures produce significant scattering, other contributions have been neglected. Thus, in the linear elastic approximation, only the scattering by the edge components of dislocations can be detected.

The long-range dilation field of an edge dislocation is smoothly varying. Fig. 1 shows calculated atomic positions within a plane normal to a centrally located edge dislocation. The atomic displacements were calculated using the isotropic linear-elastic approximation (Hirth & Lothe, 1982), which is valid outside the dislocation core region. The change in atomic density is positive in the left half of the figure and negative in the right half. Approximating this structure with interfaces separating regions with distinct electron or nuclear density is not valid. Instead, one must invoke derivations that explicitly take this smoothly varying character into account.

The coordinate system used to describe the scattering geometry is shown in Fig. 2. The dislocations extend along the Z axis and the edge components of the Burgers vectors define the X axis. Thus, the Y axis is perpendicular to the slip plane. The projection of the scattering vector onto the XY plane has length q_p and polar angle ξ. The dislocation wall must contain these dislocations and so the vector perpendicular to the wall must lie in the XY plane; this vector is labeled **t** for the 'thickness' direction. The scalar $w = |\mathbf{w}|$ is used to describe the dislocation positions within the wall 'length' direction as shown. Dipoles are modeled as two opposite-sign dislocations separated along the Y axis by a distance d (not shown in figure).

From Thomson *et al.* (1999), the kinematic scattering form factor for an individual straight dislocation with effective length H is given by

$$a_{\text{single}} \approx 4\pi b_e \kappa \frac{\sin\xi}{q_p} \frac{\sin(q_z H)}{q_z}. \quad (1)$$

Here, q_z is the Z component of the scattering vector, κ is a constant that depends only on Poisson's ratio and b_e is the edge component of the Burgers vector. The dilation field of a dislocation dipole is quite different from that of an individual dislocation and the resulting dipole scattering form factor (Thomson *et al.*, 1999) is

$$a_{\text{dipole}} \approx \frac{8\pi b_e \kappa \sin^2\xi}{q_p^{3/2}} \left(\frac{2}{\pi d}\right)^{1/2} \frac{\sin(q_z H)}{q_z}. \quad (2)$$

Equations (1) and (2) are also in agreement with earlier work by Seeger (1959*b*) and Atkinson & Hirsch (1958). An important issue in the evolution of dislocation structures is the magnitude and orientation of the dipole moment in dislocation walls (Mughrabi, 1983; Kratochvil *et al.*, 1997). The q_p dependencies in equations (1) and (2) provide a useful way to distinguish between scattering by individual dislocations and by dislocation dipoles. In particular, the squared scattering amplitude (*i.e.* the SAS intensity) of the individual dislocations exhibits a q_p^{-2} dependence whereas that by the dislocation dipoles exhibits a q_p^{-3} dependence.

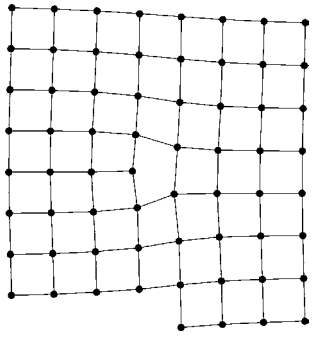

Figure 1
Approximate atomic positions in a plane perpendicular to a centrally located edge dislocation. The resulting dilation field is smoothly varying away from the dislocation core. Thus, the SAS cannot be interpreted simply in terms of scattering at interfaces between regions of differing electron or nuclear density.

The factor $\sin(q_z H)/q_z$ that appears in these equations is a function with a very strong and sharp peak at $q_z = 0$ for dislocation lengths typical of deformed metals. Thus, unless the scattering vector is very close (typically within 5 to 10°) to perpendicular to the dislocation line, no appreciable scattering will take place and the dislocation will not be visible. In this paper, the term 'visible' is used to specify the subset of dislocations that produces significant SAS. The $\sin\xi$ terms in both equations describe the effect of rotating **q** with respect to the edge component of the Burgers vector (X axis). The scattering reaches a maximum when **q** is perpendicular to the X axis. The sharpness of this maximum depends upon whether the defect is a single dislocation or a dislocation dipole. For single dislocations, the scattered intensity falls off as $\sin^2\xi$, whereas the dipole scattering falls off much more rapidly as $\sin^4\xi$. Thus, in both cases, the maximum scattered intensity is obtained when **q** is perpendicular to both the dislocation line and the edge component of the Burgers vector. This defines the slip planes of the dislocations, which, for Al at room temperature, are the {111} planes.

It is important to understand that equations (1) and (2) are both only approximate expressions with well defined regions of validity. For an individual dislocation, (1) is only valid when $qR \gg 1$ and $qR_0 \ll 1$, where R is the upper cut off for the dislocation strain field and R_0 is the effective dislocation core radius. For practical purposes, these conditions are always fulfilled in a USAXS experiment. Equation (2) for dipoles has a similar range of validity to (1), except that the core radius must be replaced by the dipole spacing. Dipole spacings in deformed f.c.c. samples vary widely, ranging from a few to several tens of nanometres. Since the scattering intensity from dipoles decreases rapidly with increasing q, the largest q for which dipole scattering might be detectable by means of our USAXS instrument is approximately 0.01 Å^{-1}. Thus, in principle, we should be able to detect the transition from a dipole to a single dislocation signature for the larger dipole separations.

The strong angular dependencies described above have important ramifications for the design and interpretation of dislocation SAS experiments. For a given beam/sample geometry, only the subset of dislocations that satisfy the above

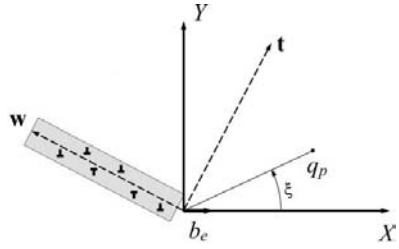

Figure 2
Coordinate system for dislocations and dislocation walls. The dislocations lie along the Z axis perpendicular to the figure at the origin and the edge component of the Burgers vector lies along the X axis. The projection of the scattering vector, **q**, in the XY plane has cylindrical coordinates (q_p, ξ). The vectors **w** and **t** are in the XY plane with **w** parallel to the wall and **t** perpendicular to the wall.

visibility conditions will contribute significantly to the SAS. Thus, since dislocations must reside on a small set of slip planes, a randomly oriented single crystal generally will exhibit very little dislocation scattering. If, instead, the crystal is oriented such that **q** is nearly perpendicular to an active slip plane, the scattering from this subset of dislocations will be maximized while the scattering from the remaining dislocations generally will be negligible.

Turning next to the different types of dislocation configurations, Thomson *et al.* (1999) explicitly considered small-angle scattering from dislocation walls. The general form predicted for the SAS intensity, I, from dislocation walls is given by

$$\begin{aligned} I &= \mathcal{A}^2[cL + F_t(q_t, L)F_w(q_w, L)] \\ \mathcal{A}_{\text{single}} &\approx \frac{4\pi\kappa}{q_p}\left(\frac{\sin(q_z H)}{q_z}\right) \\ \mathcal{A}_{\text{dipole}} &\approx \frac{8\pi\kappa}{q_p^{3/2}}\left(\frac{2}{\pi d}\right)^{1/2}\left(\frac{\sin(q_z H)}{q_z}\right), \end{aligned} \tag{3}$$

where c is a constant, L is the total visible dislocation line length, q_t is the projection of the scattering vector perpendicular to the walls, q_w is a projection along the wall and perpendicular to the visible dislocations, and $F_t(q_t, L)$ and $F_w(q_w, L)$ are factors that depend upon the dislocation configurations in the respective directions. The ξ-dependent factors from equations (1) and (2) have been included here in c, F_w and F_t, so the visibility criteria for the component dislocations remain unchanged.

$F_w(q_w, L)$ does not exhibit a simple power-law dependence on q_w; it is best described as an interference term for the partially ordered dislocation structures. $F_t(q_t, L)$, however, possesses a relatively simple monotonic q_t behavior. Thus, if the dislocation density across a wall is uniform with a sharp interface, then $F_t(q_t) \propto q_t^{-2}$. If the interface is diffuse, the scattering intensity decreases more rapidly. Following a procedure introduced by researchers investigating SAS by block co-polymers (Ruland, 1971; Koberstein *et al.*, 1980), Thomson *et al.* modeled such an interface as the convolution of a sharp interface with a Gaussian function, yielding the approximate functional form

$$F_t(q_t) \propto \frac{1}{q_t^2}(1 - \sigma^2 q_t^2), \tag{4}$$

where σ is the width of the Gaussian and corresponds to the effective width of the diffuse interface. Since q_t is a projection of the scattering vector in the direction of the wall thickness, knowledge of the orientation of the walls is required to extract the width.

If the sample/beam geometry is arranged so that q_w is appreciable, the interference term, $F_w(q_w, L)$, is highly sensitive to the ordering of the visible dislocations within the walls. Two special cases that were worked out in detail are relevant here. If we assume that $N + 1$ visible dislocations are periodically spaced with separation l/N and that all of the dislocations have the same-sign Burgers vector, then a simple diffraction grating function results with a q_w dependence given by

$$F_w(q_w) \propto \frac{\sin^2(q_w l/2)}{\sin^2(q_w l/2N)}. \tag{5}$$

An identically configured wall with alternating sign dislocations gives

$$F_w(q_w) \propto \frac{\sin^2(q_w l/2)}{\cos^2(q_w l/2N)}. \tag{6}$$

Examination of equations (5) and (6) shows that the effect of replacing every other positive dislocation with a negative dislocation is to 'shift' the diffraction pattern by half the period, or $\pi N/L$. The reason for this unusual behavior is that each positive/negative dislocation pair forms a double-sized unit cell with peaks spaced half as far apart in reciprocal space. The multiplying form factor of the dislocation pair has zeros at the *original* lattice sites, causing the apparent shift.

Thomson *et al.* also considered the case of partially ordered walls. As would be expected, the overall behavior found in equations (5) and (6) does not change.

The final term to be considered in equation (3) is cL. The constant c includes the various angular factors for the visible dislocations but it is completely independent of the dislocation configuration. It also introduces no additional q dependence beyond that of the dislocation form factors.

The SAS by dislocation walls is complicated and strongly dependent upon the dislocation configurations and the sample/beam geometry. The general behavior of the SAS, however, is readily followed using the above equations. One simple illustrative case will be explored that we will return to in §4. If we assume that q_t is appreciable, that q_w is very small and that the scattering is by individual dislocations rather than by dislocation dipoles, then the q dependence of the SAS can be written as

$$I \propto Aq^{-2} + Bq^{-4}(1 - \sigma^2 q^2), \tag{7}$$

where A and B are constants. The q^{-2} behavior comes from scattering by individual dislocations; it will be observed at a large enough q range for it to dominate over the rapidly declining contribution of the walls. At the smaller q range where the wall shape is dominant, the $q^{-4}(1 - \sigma^2 q^2)$ behavior will be observed. For finite thickness walls with infinitely sharp boundaries, $\sigma = 0$ and the q behavior becomes q^{-4}.

3. Experimental design

This section starts with a description of the USAXS instrument and a discussion of its applicability to these experiments. This is followed by brief descriptions of the samples and the *in situ* tensile stage. Next, the rotation and positioning systems that were used to control the sample/beam geometry are described. Next, potential problems are discussed along with their solutions. Finally, the general operating procedure that was used to obtain the USAXS data is described.

3.1. USAXS instrument

The Bonse–Hart-type instrument (Long *et al.*, 1991) used for the *in situ* dislocation scattering measurements reported here is a high-throughput USAXS diffractometer with a small angular step size ($\Delta q_{\min} = 4.2 \times 10^{-5}$ Å^{-1}), low minimum q ($q_{\min} = 5.5 \times 10^{-4}$ Å^{-1}), excellent wavelength resolution ($\Delta\lambda/\lambda = 5.7 \times 10^{-4}$), large sample cross-sectional area (3×3 mm) and high signal-to-noise ratio. At an incident photon energy of 7 keV ($\lambda = 1.77$ Å), the intensity at the sample position is 10^{10} photons s^{-1}. For low-contrast scattering, such as that expected from dislocation structures, a high incident photon flux is essential. The incident X-ray beam intensity from the National Synchrotron Light Source is monitored continuously, after wavelength selection by the double-crystal monochromator, by means of an He-filled transmission ionization chamber. After diffraction from the double-crystal analyzer, the scattered X-rays are detected by means of a photodiode detector with a linear response from 2000 to 2×10^{12} photons s^{-1}. Two reflections are used in the monochromator and two reflections are used in the analyzer.

The wide dynamic range of the photodiode detector enables direct measurement of the instrument profile, $R_b(q)$, with no sample in place, as well as the scattered intensity profile, $R_s(q)$, from the sample. At zero angle, the double-crystal analyzer passes the full intensity of the straight-through beam and hence the sample transmission is defined as $\mathcal{T} = R_s(0)/R_b(0)$. Scattering curves were measured from $q = 5.7 \times 10^{-4}$ to $q = 0.2$ Å^{-1}. In data reduction, $R_b(q)$ and $R_s(q)$ are treated in exactly the same manner: the photodiode detector data are corrected for dark current and detector amplification and then normalized to the monitor detector. Conversion of the scattering data into the differential scattering cross section in units of cm^{-1} sr^{-1} requires taking the ratio of the number of photons scattered per second into unit solid angle to the number of photons in the incident beam, all normalized to unit volume. The slit-smeared USAXS cross section measured by this instrument is

$$\frac{d\Sigma(q)}{d\Omega} = \frac{R_s(q)/\mathcal{T} - R_b(q)}{R_b(q)\Delta\omega_x\Delta\omega_y T}, \qquad (1)$$

where T is the sample thickness and $\Delta\omega_x$ and $\Delta\omega_y$, which define the detector solid angle Ω, are the angular width and the angular height, respectively, of the beam intercepted by the detector. For our geometry, $\Delta\omega_x = 0.02$ and $\Delta\omega_y = 2.4 \times 10^{-5}$ rad. Thus, placing the scattering data on an absolute scale requires only the measurement of T, $\mathcal{T}$, Ω and $R_b(0)$. As will be demonstrated in §4, accurate determination of sample transmission is needed to verify the integrity of the data.

3.2. Samples and tensile stage

The samples were ≈0.2 mm thick single Al (99.99+%) crystals in the shape of flat dog bones with gauge section dimensions of 3×3 mm. The short length was necessary to facilitate loading of the delicate samples. The sample width outside the gauge section was 5 mm. Such samples are thick enough to allow the evolution of 'bulk' dislocation structures and thin enough for conducting USAXS measurements at the selected photon energy of 7.0 keV (see §3.3 below). Preshaped Al single crystals with random crystallographic orientations were grown by directional solidification in a soft mold of Al_2O_3 powder. Each crystal was sliced in an acid saw to produce several dog-bone tensile specimens of identical crystallographic orientation. Samples were then chemically etched and annealed in vacuum for 48 h at 623 K.

A preliminary determination of the sample orientation was made using back-reflection Laue. The final determination of the orientation was made *in situ* with the sample mounted in the USAXS instrument.

The samples were deformed incrementally under uniaxial tension during the experiment using a computer-controlled tensile stage; the load and the relative displacement of the grips were monitored and recorded throughout the experiments. This allowed us to compare the evolving dislocation structures (as determined from the USAXS data) with the changing mechanical properties. The final plastic strain in the sample gauge section was measured in a traveling microscope after the experiment for comparison with the *in situ* strain measurements. The elastic behavior of the tensile stage was measured *ex situ* by applying an elastic load to a steel sample. This behavior was subtracted from the Al stress–strain data prior to analysis.

3.3. Sample/beam geometry

Full three-axis angular control of the scattering geometry is required for aligning **q** perpendicular to the desired slip plane (for maximum scattering contrast), for probing the relevant angular factors and for avoiding Bragg-diffraction conditions. The definitions of the laboratory-frame coordinate system are shown in Fig. 3. Although the sign of the ζ rotation does not conform to a conventional right-handed rotation system, we chose to keep this definition to maintain compatibility with the mechanical design of the equipment.

As discussed above, an X-ray wavelength of 1.76 Å (7.04 keV) and sample thicknesses of ≈200µm were used in these experiments. Each sample was first loaded into the tensile stage, which was then mounted on the rotation stage in the USAXS instrument. An X-ray video camera was used to check the position of the sample in the beam. The beam was

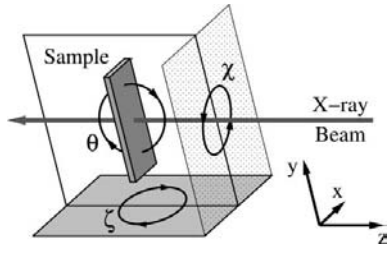

Figure 3
Laboratory-frame coordinate system along with the *xyz* Euler angles used for sample rotations. The signs of the rotations were chosen to conform to the mechanical design.

centered on the middle of the sample's gauge section. Next, the camera was used to watch the forward-transmitted beam through the sample as the sample was rotated. When a diffracting condition occurs, the sample image darkens. The measured angles where diffraction occurs can then be used to determine accurately the orientation of the sample.

With the Euler angle χ fixed, the remaining two Euler angles can be used to produce an orientation plot. This plot can be used to show the sample orientations where Bragg conditions are satisfied. Fig. 4 is an orientation plot for sample P with χ fixed at 0°. The open circles indicate measured sample orientations where Bragg diffractions were detected. The expected pattern of Bragg diffractions is calculated from the X-ray wavelength and the initial orientation data obtained using the Laue camera. Adjusting the assumed sample orientation and incident photon energy to minimize the error between the calculated and measured Bragg positions enables an accurate sample orientation and photon energy to be determined. The curved lines in Fig. 4 are the calculated Bragg positions after visually minimizing the errors. For this sample, we estimate that the 1σ error for the sample orientation is 0.2° and the beam energy is 7.04 ± 0.01 keV.

The program that calculates the positions of the Bragg diffractions also determines the correct Euler angles for aligning **q** along the ⟨111⟩ directions. The geometry of the rotation stage is such that the face of the sample must remain perpendicular to the beam to within approximately 25°. This physical restriction does not introduce unnecessary complications since larger angles would increase unacceptably the sample thickness in the beam direction. Thus, only one or two ⟨111⟩ directions can be aligned parallel to **q** for a given sample.

Fortunately, aligning **q** perpendicular to a specified {111} slip plane does not fully specify the orientation of the sample since rotation about this ⟨111⟩ direction is allowed. The control program calculates the Euler angles corresponding to rotations about this axis, taking into account the physical restrictions. These possible angles are then compared with the positions of the Bragg diffractions, and orientations are chosen that generally are at least 3° away from the nearest diffraction. If no suitable orientations are possible for a given slip plane, then small variations in the photon energy can be used to modify the positions of the Bragg diffractions.

Two orientations, (ζ, θ, χ), of sample P that align **q** perpendicular to the $(\bar{1}1\bar{1})$ slip plane while avoiding interference from Bragg diffractions are **F** = (0°, 1.7°, 60.2°) and **J** = (−13.7°, 0.8°, 59.7°). Since the difference in χ between these orientations is small, **F** and **J** can both be shown on a two-dimensional plot where $\chi = 60.2°$; see Fig. 5. Several orientations that are referred to in this paper are shown along with the calculated and measured diffraction positions.

3.4. Problems and solutions

The experiments were designed to obtain dislocation USAXS data from high-purity single-crystal Al. Defects such as vacancies and clusters of vacancies that form during deformation (for example by jog motion) do not contribute significantly to the scattering at the ultra-low q range ($0.0005 \leq q \leq 0.005$ Å^{-1}) examined in these experiments. Besides dislocations, the only other possible sources of scattering in this range are double Bragg (kinematic) diffraction (Beeman *et al.*, 1957; Atkinson & Lowde, 1957; Warren, 1959; Ogier *et al.*, 1959) and surfaces (Robinson & Smoluchowski, 1956; Roth, 1977; Henderson, 1995). X-ray fluorescence from surface contaminants (Freize *et al.*, 1960; Parker, 1972) would be eliminated by the analyzer crystals. Both of these possible spurious scattering sources have been investigated and the methods that were used to avoid them are described in this subsection.

Since we cannot use wavelengths long enough to eliminate all Bragg reflections, we selected a wavelength long enough to avoid most Bragg reflections and still compatible with

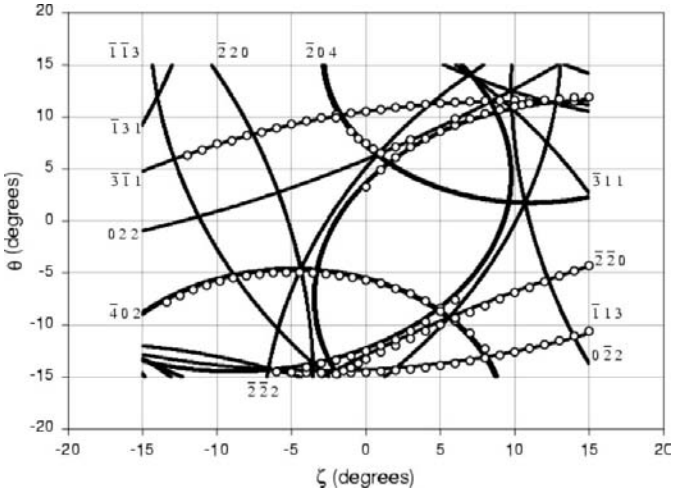

Figure 4
Orientation plot for sample P with $\chi = 0°$. The curved lines show the calculated orientations where the indicated Bragg reflections are expected to occur and the data points indicate orientations where Bragg reflections were observed. The width of the curved line reflects the width of the reflection assuming isotropic peak shapes.

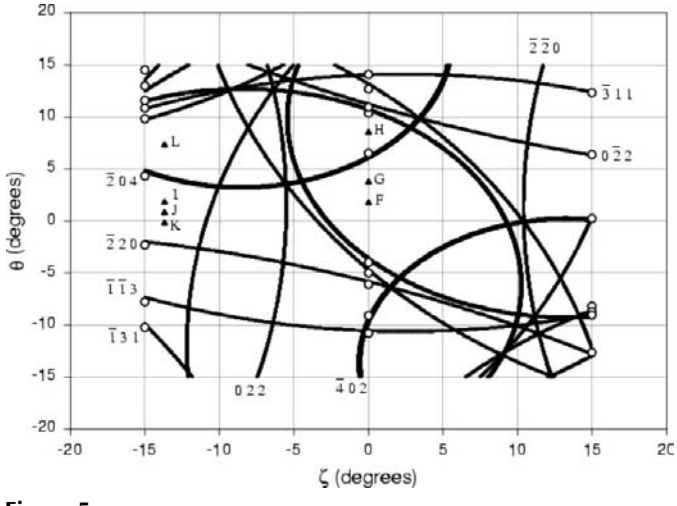

Figure 5
Orientation plot for sample P with $\chi = 60.2°$. The open circles indicate orientations where Bragg reflections were observed. The solid triangles indicate orientations where USAXS data were obtained.

reasonable transmission through the sample. The remaining reflections were avoided by controlling the crystallographic orientation of the sample with respect to the incident beam. For undeformed single-crystal samples, such avoidance is straightforward because the Bragg diffractions are narrow; the problem becomes more difficult when the deformation reaches several percent, the Bragg peaks broaden considerably (Mughrabi, 1983; Ungar *et al.*, 1982; Yuming *et al.*, 1982; Ungar *et al.*, 1984; Mughrabi *et al.*, 1986; Biermann *et al.*, 1991; Ungar *et al.*, 1991, 1993; Ungar, 1994; Ji *et al.*, 1994; Ungar & Borbely, 1996; Wilkens, 1970*a*,*b*; Krivoglaz, 1996; Levine & Thomson, 1997; Schafler *et al.*, 2005) and sample rotations occur (Honeycombe, 1968; Hughes *et al.*, 1998).

The effects of Bragg diffractions on USAXS data were investigated at both small and large strains. We demonstrate below that (i) avoidance of Bragg diffractions is possible, (ii) the excess scattering from double Bragg diffraction does not resemble the predicted and measured USAXS profile of dislocation walls, and (iii) it is possible to detect the intrusion of Bragg diffractions in the USAXS data.

Fig. 6 shows absolute-calibrated slit-smeared USAXS data from six orientations (**C**, **E**, **F**, **G**, **H** and **I**) of sample *O*. USAXS scans from all orientations that were at least 0.5° away from Bragg reflections (**E**, **F**, **G**, **H** and **I**) are nearly indistinguishable. Excess scattering is apparent in the scan from orientation **C** which was within 0.2° of a Bragg reflection. Scans from other orientations very close to Bragg reflections show similar excess scattering, which we attribute to double Bragg diffraction. The double Bragg scattering varies in magnitude, but each of the intensity profiles exhibits power-law behavior, with equivalent desmeared slopes ranging from −2.7 to −3.1. Thus, none of the measured intensity profiles approaches the q^{-2} dependence predicted for SAS by individual dislocations, and the angular dependence is very different from that expected from SAS by dislocation dipoles, which is discussed further below.

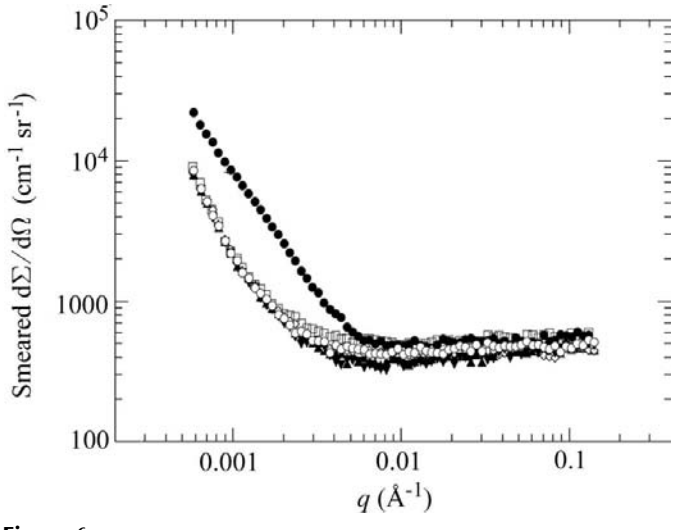

Figure 6
Absolute-calibrated USAXS data from sample *O* with 0% applied strain. Orientations **E** (open square) through **I** (upward filled triangle, open diamond, inverted filled triangle and open circle) are rotated at least 0.5° away from Bragg reflections and orientation **C** (filled circle) is within 0.2° of a Bragg reflection.

As described in §3.1, the incident-beam intensity was monitored continuously during each USAXS scan and the photodiode signal is normalized accordingly. Further, a direct measurement of the sample transmission is available from the data (as described in §3.1), which allows the average sample thickness to be calculated. Since the orientation of the sample is known, the resulting geometrical corrections arising from sample tilt can be used to determine the true sample thickness, T_0, perpendicular to the face. Since Bragg diffraction directs intensity away from the photodiode, it reduces the measured transmission coefficient, resulting in an increased (spurious) value for T_0. Since the USAXS intensity is only sensitive to double Bragg scattering and the transmission coefficient is sensitive to single Bragg scattering, the transmission measurement should be able to detect the intrusion of Bragg diffraction before it becomes significant in the USAXS data.

Calculating T_0 for sample *O*, orientations **E** through **I**, gives $T_0 = 201.2 \pm 0.2$ μm, with a standard uncertainty for an individual measurement of 0.5 μm. As shown in Fig. 6, these orientations show no evidence of double Bragg diffraction. Calculating T_0 using all orientations that do show such evidence gives $T_0 = 203.2 \pm 0.4$ μm, with a standard uncertainty for an individual measurement of 1.1 μm. As predicted, the presence of Bragg diffraction significantly increases the measured value for T_0. Orientation **C** shows the strongest double Bragg signature in the USAXS data and also has the largest measured $T_0 = 204.3$ μm.

For another sample, *G*, USAXS data were taken from a single sample orientation for engineering strains ranging from 0 to 8%. Fig. 7 shows T_0 plotted as a function of the measured engineering strain for this sample. As expected, the sample thickness decreases linearly with strain at small strains; at larger strains, the slope of the curve decreases as deformation occurs outside the gauge section of the sample. After removal of the sample from the tensile stage, surface slip structures (indicative of plastic strain) were observed outside the gauge section. As the sample is deformed, sample rotation and Bragg-peak broadening occur. Thus, the departure from a

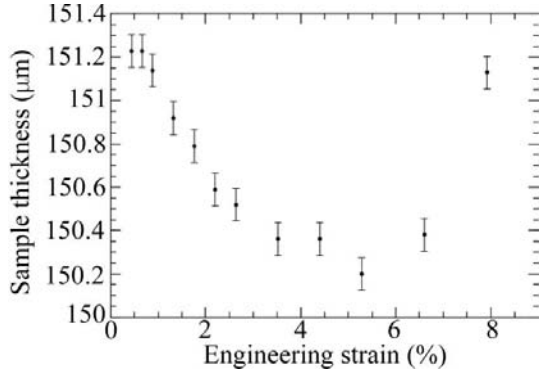

Figure 7
Sample thickness, as derived from the sample transmission, plotted as a function of the measured engineering strain. The abrupt increase that occurs above 6% strain is attributed to an encroaching Bragg peak.

smooth monotonic behavior that occurs above 6% strain is attributed to encroaching Bragg conditions. Examination of the USAXS data from sample *G* shows a slope change in the scattering data taken at 8% strain that is consistent with the intrusion of double Bragg diffraction. Similar evidence does not appear in the scan taken at 6.7% strain, demonstrating that contamination by double Bragg diffraction is not significant. The sample transmission at 6.7% strain does show clear evidence of single Bragg diffraction, demonstrating that this method is sufficiently sensitive to detect double Bragg diffraction before it becomes large enough to affect the USAXS data.

The possibility of observing scattering from improperly prepared surfaces is another consideration. Parasitic surface scattering has been attributed to surface oxide films (Robinson & Smoluchowski, 1956), damage layers from cold rolling (Robinson & Smoluchowski, 1956) and surface irregularities (Roth, 1977) such as saw marks and scratches. Many of these conditions can be avoided by careful preparation of sample surfaces. For example, surface etching, such as was used for our samples, has been proven (Freize *et al.*, 1960; Parker, 1972; Henderson, 1995) to reduce significantly the possibility of surface small-angle scattering. Microscopic examinations of the surfaces of the strained single-crystal samples used in this study revealed the existence of small (<1 μm) surface facets and only rare features as large as 2.5 μm. The observed scattering cannot be understood in terms of scattering by these features. In the case of Al, the presence of a thin oxide film is unavoidable for measurements conducted in air, but Porod scattering from such films cannot be observed at scattering vectors $q < 0.001$ Å^{-1}, which is where the Porod scattering that we attribute below to dislocation walls is observed. Porod scattering has been observed (Roth, 1977) around 0.02 Å^{-1}, implying that the oxide layer thickness may be of the order of 100 Å.

In a final demonstration that the observed scattering results from internal dislocation structures, several samples described in this study were re-examined after a room-temperature anneal of several months. The dislocation dipole signatures remained, while the scattering from individual dislocations decreased significantly. Such behavior is expected from high-purity Al samples.

An additional candidate for Porod scattering is the geometrical cross section of the sample. Scattering from the geometrical cross section has been observed (Roth, 1977) from thin (75 μm) samples. Such scattering from an imperfect external surface perpendicular to the incident beam depends on the value of the total area of the projection of this surface onto a plane parallel to the incident beam, where q is perpendicular to the incident beam. Thus, when the sample is unstrained and the incident X-ray beam is exactly along the surface normal, there is minimal Porod scattering from the surface. The possibility of scattering from the sample cross section was examined using data from undeformed sample *O*, which was measured to be 201.6 ± 0.3 μm thick. As discussed above, this sample was oriented for low dislocation scattering contrast. Porod scattering was observed at orientation **F**, nominally 6° from the normal, and at orientation **I**, nominally 12° from the sample normal. The scattering is almost identical, which is consistent with scattering by structures within the volume of the sample (such as low-contrast contributions from multiple dislocation walls). If the scattering was caused by the sample surfaces, it would change by a factor of two. The lack of such angular dependence was also observed in the scattering profiles from other samples.

3.5. Experimental procedure

After a sample was crystallographically oriented *in situ*, sample orientations for USAXS data acquisition were selected. USAXS data were first obtained from the unstrained sample. The sample was then strained to a predetermined level at a strain rate of 0.01% s^{-1} and additional USAXS scans were taken. The stress on the sample was maintained just below the flow stress (≈ 0.99) while holding at a specific strain. This straining and scanning process was repeated for several levels of strain. Unless otherwise specified, the cross-sectional area of the beam on the gauge section was 2×2 mm. Using an X-ray video camera, the sample position was adjusted before each scan so that the X-rays sampled the same volume throughout the *in situ* experiment. A microscopic examination of each sample was conducted following each USAXS experiment. No dimensional instabilities were observed, demonstrating that the macroscopic strains were nearly isotropic.

4. *In situ* USAXS results

The results presented here are intended to demonstrate the effectiveness of the technique and to provide experimental validation of Thomson *et al.* (1999). The USAXS data presented in this section were obtained from four Al single crystals, deformed *in situ* as described in §3. The first two crystals (*P* and *Q*) were oriented for high dislocation SAS contrast, with **q** aligned perpendicular to slip planes with active slip systems. The third crystal (*G*) was oriented such that **q** was still nearly perpendicular to a large population of dislocations but not perpendicular to the edge components of their Burgers vectors (medium contrast). The resulting USAXS data from these orientations show pronounced changes in dislocation structure throughout the *in situ* experiments and quantitative results can be extracted. Some of the predicted angular dependencies are also investigated. Finally, data are presented from a fourth crystal (*J*) that was oriented such that dislocation SAS contrast was low. The experimental results are consistent with the theoretical predictions discussed in §2. Table 1 lists information relevant to the samples for reference.

4.1. High contrast orientations

Results from sample *P* are presented first. This sample was deformed uniaxially in tension along [0.66 0.42 0.62]. The sample orientations from which data are presented are shown

Table 1
Sample information.

Sample	Strain axis	Strain range	Orientation	Desmeared power law	Dislocation type†
P	[0.66 0.42 0.62]	10%	(0.0°, 1.7°, 60.2°) (−13.7°, 0.8°, 59.7°)	−2 and −4	*s*, *w*
Q	[−0.85 −0.49 0.18]		(10.1°, −24.4°, −20.4°)	−2.3	*m*
			(10.1°, −25.4°, −20.4°)	−3	*d*
			(10.1°, −26.4°, −20.4°)	−2	*s*
G	[0.03 0.85 −0.53]	0.4–6.7%		−2	*s*, *w*
J	[0.03 0.85 −0.53]	5.8–11.7%			*w*

† *s* = single, *d* = dipole, *m* = mixed, *w* = wall.

in Fig. 5. As mentioned previously, orientations $\mathbf{F} = (0^\circ, 1.7^\circ, 60.2^\circ)$ and $\mathbf{J} = (-13.7^\circ, 0.8^\circ, 59.7^\circ)$ align the $(\bar{1}1\bar{1})$ slip plane perpendicular to **q**, while avoiding the intrusion of Bragg peaks. Using X-ray transmission measurements from non-diffracting orientations, the average starting thickness of the sample was determined to be 196.8 ± 0.6 μm.

Fig. 8 shows absolute-calibrated slit-smeared USAXS data from orientation **F** at 10% applied strain. For comparison, the theoretical slit-smeared slopes equivalent to −2 for scattering from individual dislocations and −4 for scattering from sharp dislocation walls are also shown. The observed slopes are in agreement with the theoretical predictions (see §2), where there is evidence of scattering by dislocation walls and single dislocations. The peak structure in Fig. 8 demonstrates the presence of spatially ordered dislocations. The data are consistent with a low-angle tilt boundary with a misorientation of about 0.09°.

The next sample, *Q*, was deformed uniaxially in tension along [−0.85 −0.49 0.18]. Comparisons at different strain can only be made if the same scattering volume is used for each of the measurements. In the experiments reported here, the beam is positioned on the sample with an accuracy of 10 μm before each scan is made. Since changing the sample orientation changes the projection of the beam onto the sample, perfect volume matching is impossible, but we estimate the resulting volume mismatch for a 10° sample rotation to be less than 1%. Orientation $\mathbf{A} = (10.1^\circ, -24.4^\circ, -20.4^\circ)$ aligns the $(\bar{1}\bar{1}1)$ slip plane perpendicular to **q**, while avoiding interference from Bragg peaks. Recall also that single-crystal samples rotate during straining, so orientation **A** slowly shifts position with respect to the crystal axes. As we describe below, this shifting was followed throughout the later stages of the straining process.

As discussed in §2, dislocation SAS theory predicts $\mathcal{A}^2 \propto q^{-2}$ for single dislocations and $\mathcal{A}^2 \propto q^{-3}$ for dislocation dipoles [see equation (3)]. Fig. 9 shows USAXS scans taken from orientations in sample *Q* of **A**, **H** and **M** at 6% strain. Orientations **H** and **M** are obtained by rotating the sample away from **A** by −1 and −2°, respectively, in the ζ direction. As mentioned previously, rotation occurs during straining; at this strain, orientation **H** aligns **q** perpendicular to the $(\bar{1}\bar{1}1)$ slip planes. Fitting a power law to the data from **H** gives a desmeared slope of -3.00 ± 0.05. This slope demonstrates that a significant number of dislocations are arranged in dipole configurations. Rotating just ±1° from this orientation, so that **q** is no longer perpendicular to the $(\bar{1}\bar{1}1)$ slip planes, produces the lower scans shown in Fig. 9 with fitted desmeared slopes of −2.3 for **A** and −2.0 for **M**. Additional rotation returns the orientation **A** slope to −2.0. The rapid loss of the dipole signature confirms the theoretical prediction of strong angular dependencies of the scattering. The angular range of the q^{-2} scattering is much broader. From the predicted functional

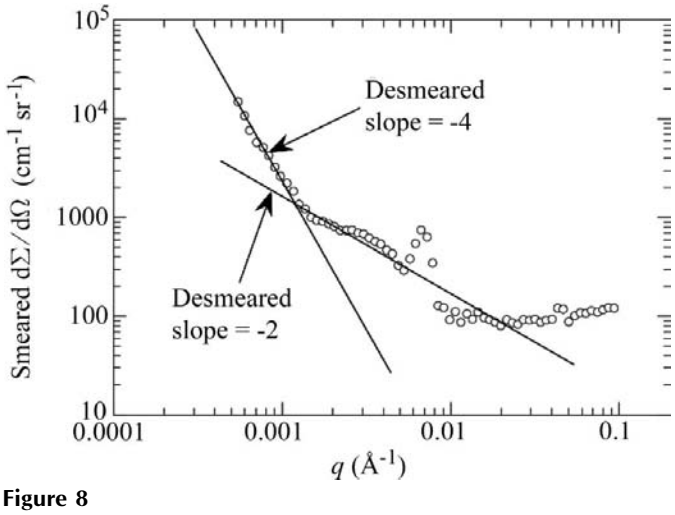

Figure 8
Slit-smeared ultra-small-angle X-ray scattering data from sample *P*, strained *in situ* to 10% strain. The straight lines indicate the predicted desmeared slopes from dislocation wall SAS. The peak structure is produced by correlations in the dislocation spacing.

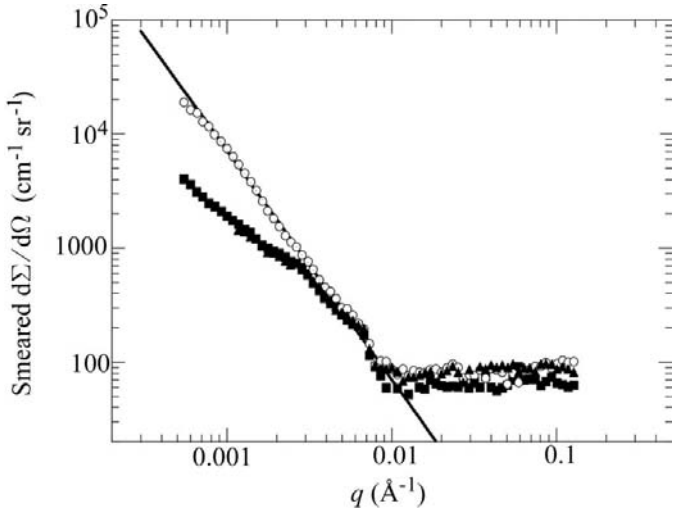

Figure 9
Slit-smeared ultra-small-angle X-ray scattering data taken at three orientations just 1° apart from sample *Q* at 6% strain. Filled squares represent data from orientation **A** ($\theta = -24.42^\circ$), open circles represent data from orientation **H** ($\theta = -25.42^\circ$), and filled triangles represent data from orientation **M** ($\theta = -26.42^\circ$). The desmeared q^{-3} slope demonstrates the presence of dislocation dipoles in the sample.

form for $\mathcal{A}^2_{\rm dipole}$ in equation (3), we thus obtain a lower limit of $H = 3$ μm for the length scale over which the dipoles satisfy the visibility requirements. Such long lengths are consistent with dislocations trapped by geometrically necessary boundaries (Hughes *et al.*, 1998) or large cell walls. The high-q end of the dipole scattering in Fig. 9 exhibits a decreasing slope, starting at approximately $q = 0.004$ Å^{-1}. This gives an upper limit of about 20 nm on the dipole separation. Once again, additional information concerning the orientation of the dipoles is required to extract further quantitative results such as the ratio of dipoles to individual dislocations. More extensive rotation data should allow these factors to be determined.

4.2. Medium contrast orientations

Sample G was placed in an orientation that was not perpendicular to a primary slip plane, yet still exhibited significant excess scattering. Thus, out of several attempts, this was the only sample where we succeeded in locating a non-slip plane orientation where **q** remained nearly perpendicular to a significant number of dislocations. No further rotations were attempted on this sample; instead, the USAXS was measured for a single orientation at applied strains of 0, 0.2, 0.4, 0.7, 0.9, 1.3, 1.8, 2.2, 2.7, 3.6, 4.4, 5.3, 6.7 and 8.0%. The sampled volume was 2 mm × 2 mm × 51 μm.

Within an angular error of approximately 0.5°, both the tensile axis and the scattering vector for sample G were [0.03 0.85 −0.53] . This scattering vector was approximately 3° away from the nearest Bragg diffraction.

To interpret the scattering results, information on the orientations of the visible dislocations and dislocation walls is needed. The requirement that the dislocation lines reside on slip planes means that they are perpendicular to ⟨111⟩ directions in the crystal. Calculating the resulting $\sin^2(\xi)$ for all four possible slip planes gives 0.04 for (111), 0.61 for $(\bar{1}1\bar{1})$, 0.66 for $(\bar{1}\bar{1}1)$, and 0.03 for $(1\bar{1}\bar{1})$. Thus, the visible dislocations must lie on either the $(\bar{1}1\bar{1})$ or $(\bar{1}\bar{1}1)$ slip planes. These are also the slip planes with the highest (and nearly equal) resolved shear stresses; the relevant Schmid factors are 0.42 for $[101](\bar{1}1\bar{1})$ and 0.37 for $[110](\bar{1}1\bar{1})$.

To determine the geometry of the wall structures, an *in situ* high-resolution diffraction imaging experiment using monochromatic topography (Kuriyama *et al.*, 1982) was conducted on an identically oriented single-crystal tensile specimen (Levine *et al.*, 2000). The resulting images showed that the dislocations formed wall structures parallel to the $(\bar{1}\bar{1}1)$ and $(\bar{1}1\bar{1})$ slip planes. Such structures have been observed previously in *ex situ* transmission-electron-microscope studies of deformed f.c.c. metals and are usually referred to as dislocation carpets (Steeds, 1966).

Fig. 10 shows the absolute-calibrated slit-smeared USAXS intensity plotted as a function of q for strain values of 0.4, 0.9, 2.2, 3.6, 4.4, 5.3 and 6.7%. Each scan exhibits two straight lines that intersect near $q = 0.001$ Å^{-1}. As for sample P, the data at larger q (around 0.001 to 0.01 Å^{-1}) have a slit-desmeared equivalent slope of −2 and correspond to scattering from individual dislocations. The changing height of the −2 slope region indicates that the visible dislocation content is increasing with strain. As discussed previously, the smaller-q scattering is attributed to the distribution of dislocations in the thickness direction of the walls and these structures are observed in all of the scans of sample G except for the first two at 0 and 0.2% strain. To extract the width of the wall/channel interface, σ, from the desmeared smaller-q USAXS data, we first fitted the larger-q data with a power law and subtracted this function from the smaller-q data. This subtraction effectively removed the first term from equation (7). Fitting the resulting data with the function given by equation (4) and including the appropriate projection for q_t allows us to extract the width, σ_t, of the interface region in the direction perpendicular to the dislocation walls. The behavior of this width will be discussed further below.

4.3. Low contrast orientations

All of the above results were obtained from crystals oriented for high or medium dislocation scattering contrast. It is useful to compare these results with USAXS data from identical crystals with different orientations. The very sharp angular dependence predicted by equations (1) and (3) suggests that dislocation scattering should be undetectable for most sample orientations. However, USAXS data from all of the samples that were rotated for low dislocation scattering contrast show a barely detectable scattering profile consistent with dislocation scattering. The presence of this small excess scattered intensity is not surprising, since dislocations generally form complete loops of complicated shapes. Thus, for any sample/beam geometry, some small fraction of the total dislocation line length in the sample will always be perpendicular to **q**. Of course, the edge component of the Burgers vectors will not generally be perpendicular to **q**, but this

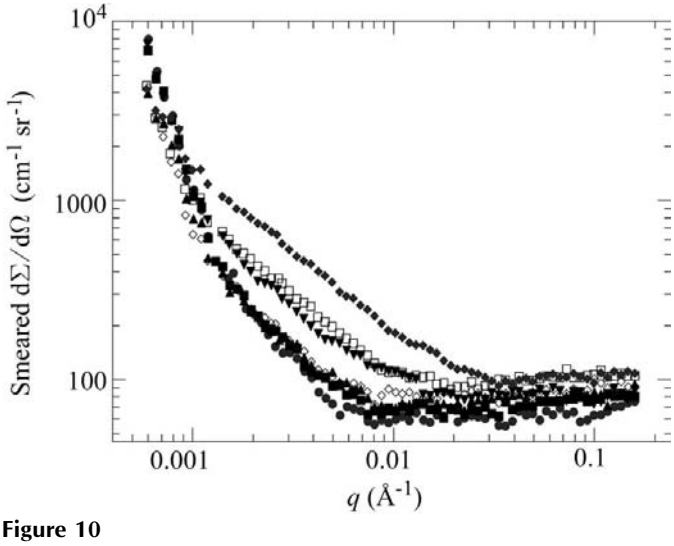

Figure 10
Slit-smeared ultra-small-angle X-ray scattering data from sample G at strains of 0.4% (filled circles), 0.9% (filled squares), 2.2% (filled triangles), 3.6% (open diamonds), 4.4% (inverted filled triangles), 5.3% (open squares) and 6.7% (filled diamonds).

angular dependence is much more slowly varying, and will not completely eliminate the dislocation scattering.

Sample *J* has the same crystallographic orientation as sample *G*, but USAXS data were obtained from a different sample orientation that still avoids Bragg scattering.

As discussed above, the low-*q* USAXS data from sample *G* exhibited changes that were consistent with a sharpening interface of the dislocation walls with increasing strain. Although the scattering intensity from sample *J* is much smaller than from sample *G*, the low-*q* USAXS data show similar behavior and the interface width can be extracted using the same procedure. For sample *G*, **q** was symmetrically oriented with respect to both possible wall orientations, so the true interface width, σ_t, could be extracted. For sample *J*, however, the projections for the $(\bar{1}1\bar{1})$ and $(\bar{1}\bar{1}1)$ dislocation walls are different (0.77 and 0.86, respectively). Fig. 11 shows the extracted interface widths using both possible projections for sample *J* along with the σ_t values obtained from sample *G*. The data from both samples fit smoothly together, demonstrating that the same sets of dislocation walls are being sampled in the two crystallographically identical samples. Since both wall projections for sample *J* are consistent with the sample *G* data, no distinctions can be made between them. The combined data show that the width of the interface region decreases approximately linearly with increasing strain. Theoretical models of work hardening are just now starting to consider the role of such evolving dislocation density gradients (Mughrabi, 2001); at present, USAXS provides the only viable experimental technique for measuring this parameter *in situ*.

5. Conclusions

This paper presents the first measurements of dislocation wall structure using SAS. The USAXS measurements were conducted on samples of single-crystal Al, deformed *in situ* by uniaxial tension. Since dislocation SAS is a low-contrast scattering process, great care was taken to avoid higher-contrast processes such as double Bragg diffraction. Other potential problems such as surface scattering and scattering from contaminants also were carefully avoided. In §3.4, we described in detail the steps taken to avoid these difficulties and the experimental measurements that were made to confirm that these effects were properly understood.

The experimental results presented in this paper serve as a test of the theory of small-angle scattering from dislocation walls as developed by Thomson *et al.* (1999). It is noteworthy that all of the scattering features predicted by the theory were observed and that the quantitative results extracted using this theory have reasonable values. Particularly important (and also potentially quite valuable) is the selective nature of the USAXS probe. Orienting the scattering vector perpendicular to a given slip plane maximizes the scattering from this set of dislocations while minimizing the contribution from the conjugate slip systems. For this reason, USAXS cannot be used to measure the total dislocation content of a sample. Instead, USAXS may be used for the purpose of comparing well defined subsets of dislocations that develop and evolve as a sample deforms plastically.

Successful *in situ* dislocation USAXS experiments require an ultra-low $q_{\min}$ ($<10^{-3}$ Å^{-1}) with small Δq ($\leq 10^{-4}$ Å^{-1}), a high photon flux and complete angular control of single-crystal metal samples. Although difficult to conduct, dislocation USAXS provides many useful capabilities including the ability to examine dislocation structures in bulk materials. Dislocation USAXS can also provide measurements of physical parameters that cannot be determined *via* any other available experimental technique.

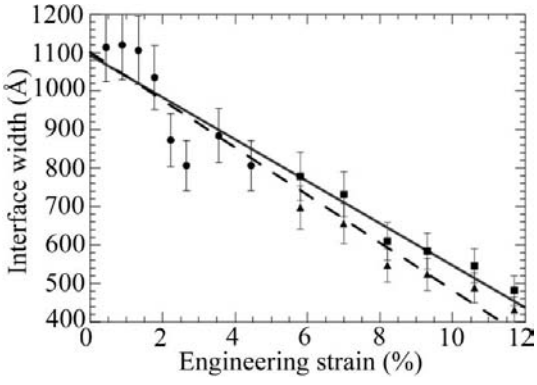

Figure 11
Extracted true interface widths of dislocation wall boundaries in crystallographically identical samples *G* and *J* plotted as a function of strain. The circles were extracted from the sample *G* data, and the triangles and squares were extracted from the sample *J* data, using $(\bar{1}1\bar{1})$ and $(\bar{1}\bar{1}1)$ projections, respectively. The solid line is a linear fit using the $(\bar{1}1\bar{1})$ *J* data along with the sample *G* data. The dashed line uses the $(\bar{1}\bar{1}1)$ *J* data along with the sample *G* data.

We thank H. E. Burdette for measuring the orientation of our single-crystal samples using Laue diffraction. The experiments reported in this paper were conducted using the USAXS facility at the National Institute of Standards and Technology's materials science beamline (X23A3) at the National Synchrotron Light Source at Brookhaven National Laboratory. The NSLS is operated under contract No. DE-AC02-76CH00016 with the US Department of Energy.

References

Atkinson, H. H. & Hirsch, P. B. (1958). *Philos. Mag.* **3**, 476–488.
Atkinson, H. H. & Lowde, R. D. (1957). *Philos. Mag.* **2**, 589–590.
Beeman, W. W., Kaesberg, P., Anderegg, J. W. & Webb, M. B. (1957). *Handb. Phys.* **32**, 321–442.
Biermann, H., Kugn, H.-A., Ungar, T., Hammer, J. & Mughrabi, H. (1991). *Proc. ICSMA 9*, edited by D. G. Brandon, R. Chaim & A. Rosen, London: Freund Publishing Company Ltd.
Blin, J. & Guinier, A. (1951). *C. R. Acad. Sci.* **233**, 1288–1290.
Blin, J. & Guinier, A. (1953). *C. R. Acad. Sci.* **236**, 2150–2152.
Christ, J. (1964). *Phys. Status Solidi*, **7**, 557–576.
Dexter, D. (1953). *Phys. Rev.* **90**, 1007–1012.
Freize, E. J., Fine, M. E. & Kelly, A. (1960). *Philos. Mag.* **5**, 101–103.
Hayes, S. & Smoluchowski, R. (1954). *Appl. Sci. Res.* B**4**, 10–24.
Henderson, S. J. (1995). *J. Appl. Cryst.* **28**, 820–826.
Heuser, B. J. (1994). *J. Appl. Cryst.* **27**, 1020–1029.
Hirth, J. & Lothe, J. (1982). *Theory of Dislocations*. New York: Wiley.

Honeycombe, R. W. K. (1968). *The Plastic Deformation of Metals*. New York: St Martin's Press.
Hughes, D. A., Chrzan, D. C., Liu, Q. & Hansen, N. (1998). *Phys. Rev. Lett.* **81**, 4664–4667.
Ji, N., Lebrun, J. L. & Sainfort, P. (1994) *J. Mater. Sci.* **29**, 1553–1557.
Kettunen, P., Lepistö, T., Kostorz, G. & Göltz, G. (1981). *Acta Metall.* **29**, 969–972.
Koberstein, J. T., Morra, B. & Stein, R. S. (1980). *J. Appl. Cryst.* **13**, 34–45.
Kratochvil, J., Saxlova, M., Devincre, B. & Kubin, L. P. (1997). *Mater. Sci. Eng.* A**234**, 318–321.
Krivoglaz, M. A. (1996). *X-ray and Neutron Diffraction in Nonideal Crystals*. Berlin: Springer.
Kuriyama, M., Boettinger, W. J. & Cohen, G. G. (1982). *Ann. Rev. Mater. Sci.* **12**, 23–50.
Lepistö, T. K., Kostorz, G., Kuokkala, V.-T. & Kettunen, P. (1991). *Mater. Sci. Eng.* A**131**, 171–176.
Levine, L. E., Long, G. G. & Black, D. R. (2000). In *Multiscale Phenomena in Materials: Experiments and Modeling*, edited by D. H. Lassila, I. M. Robertson, R. Phillips & B. Devincre, MRS Proc., Vol. 578, pp. 73–85. Warrendale: Materials Research Society.
Levine, L. E. & Thomson, R. (1997). *Acta Cryst.* A**53**, 590–602.
Long, G. G., Jemian, P. R., Weertman, J. R., Black, D. R., Burdette, H. E. & Spal, R. (1991). *J. Appl. Cryst.* **24**, 30–37.
Mughrabi, H. (1983). *Acta Metall.* **31**, 1367–1379.
Mughrabi, H. (2001). *Mater. Sci. Eng.* A**317**, 171–180.
Mughrabi, H., Ungar, T., Kienle, W. & Wilkens, M. (1986). *Philos. Mag.* A**53**, 793–813.
Ogier, W. T., Wild, R. L. & Nickel, J. C. (1959). *J. Appl. Phys.* **30**, 408–412.
Parker, B. A. (1972). *J. Appl. Cryst.* **5**, 372–373.
Robinson, W. H. & Smoluchowski, R. (1956). *J. Appl. Phys.* **27**, 657–658.
Roth, M. (1977). *J. Appl. Cryst.* **10**, 172–176.
Ruland, W. (1971). *J. Appl. Cryst.* **4**, 70–73.
Schafler, E., Simon, K., Bernstorff, S., Hanak, P., Tichy, G. Ungar, T. & Zehetbauer, M. J. (2005). *Acta Mater.* **53**, 315–322.
Seeger, A. (1959*a*). *Z. Naturforsch. Teil A*, **14**, 74–80.
Seeger, A. (1959*b*). *J. Appl. Phys.* **30**, 629–637.
Seeger, A. & Brand, P. (1965). *Small Angle Scattering*, edited by H. Brumberger. New York: Gordon and Breach.
Steeds, J. W. (1966). *Proc. R. Soc. London Ser. A*, **292**, 343–373.
Taglauer, E. (1968). *Phys. Status Solidi*, **29**, 259–268.
Thomson, R., Levine, L. E. & Long, G. G. (1999). *Acta Cryst.* A**55**, 433–447.
Ungar, T. (1994). *Mater. Sci. Forum*, **166–169**, 23–44.
Ungar, T., Biermann, H. & Mughrabi, H. (1993). *Mater. Sci. Eng.* A**164**, 175–179.
Ungar, T & Borbely, A. (1996). *Appl. Phys. Lett.* **69**, 3173–3175.
Ungar, T., Mughrabi, H., Rönnpagel, D. & Wilkens, M. (1984). *Acta Metall.* **32**, 333–342.
Ungar, T., Mughrabi, H. & Wilkens, M. (1982). *Acta Metall.* **30**, 1861–1867.
Ungar, T., Mughrabi, H., Wilkens, M. & Hilscher, A. (1991). *Philos. Mag.* A**64**, 495–496.
Warren, B. E. (1959). *Acta Cryst.* **12**, 837–841.
Wilkens, M. (1970*a*). *Fundamental Aspects of Dislocation Theory*, edited by J. A. Simmons, R. deWit & R. Bullough. *Natl Bur. Stand. (US) Spec. Publ.* No. 317, pp. 1191–1193, 1195–1221.
Wilkens, M. (1970*b*). *Phys. Status Solidi A*, **2**, 359–370.
Yuming, W., Shansan, L. & Yenchin, L. (1982). *J. Appl. Cryst.* **15**, 35–38.